The influence of different preparation methods on the erosion behavior of NiP-ZrO$_2$ nanocomposite coating

Mostafa H. Sliem [a,1], Osama Fayyaz [a,1], R.A. Shakoor [a,c,*], Sara Bagherifard [b], Bilal Mansoor [d,e], Aboubakr Abdullah [a], Adel Mohamed Amer Mohamed [f]

[a] *Center for Advanced Materials, Qatar University, Doha, 2713, Qatar*
[b] *Department of Mechanical Engineering, Politecnico di Milano, Milano, Italy*
[c] *Department of Mechanical and Industrial Engineering, College of Engineering, Qatar University, 2713, Doha, Qatar*
[d] *Mechanical Engineering Program, Texas A&M University at Qatar, Qatar*
[e] *Department of Materials Science and Engineering, Texas A&M University, College Station, TX 77843, USA*
[f] *Department of Metallurgical and Materials Engineering, Faculty of Petroleum and Mining Engineering, Suez University, Suez 43721, Egypt*

A B S T R A C T

Three different deposition techniques were utilized to synthesize NiP-ZrO$_2$ nanocomposite coatings. The structural and mechanical merits for the as-prepared coatings were compared through XRD, XRF, SEM, AFM, microhardness, and nanoindentation analysis. The pulse-electrodeposition was the most suitable technique with a hardness value of 653HV$_{25}$. The erosion behavior for the different NiP-ZrO$_2$ coatings was investigated based on erosion duration, particles velocity, and impact angle. The results shows that the erosion rate decreases linearly with increasing angle of incidence and increases with increasing particle velocity. The erosion mechanism is mainly fracturing of splats and ploughing action at low particle velocity due to the ductility merits of the different coatings. In contrast, larger craters, radial cracks, and micro cuttings were observed at higher speeds.

1. Introduction

Erosion is a severe material degradation that occurs when a dynamic solid particle impinges on the target and removes material due to its collision with the surface of machinery and equipment [1–3]. The process produces negative outcomes such as part wear, roughening of the surface, macroscopic scooping appearance, surface deterioration, and a decrease in the structure's functional life. It degrades the efficiency of mechanical components such as steam turbines, rocket motor tail nozzles, gas turbine blades, helicopter rotors, and pipeline systems carrying slurry and fluid [4–6]. Considerable efforts have been made to minimize the severe financial and environmental consequences of erosion in various industries, especially in oil and gas transportation systems. As a result, utilization of product specific surface modification techniques that provide improved erosion resistance appears to be a promising solution [7–10]. Despite the fact that several methods for pipe security have been proposed, internal coatings have proven to be the most reliable. In industry, fusion bonded epoxy, polymer tapes, and a variety of composite coatings are examined, but each has its own set of limitations. Some of these coatings have been restricted in their use due to coating adhesion, expense, and safety concerns. As a result, creating a new inner coating technology that will provide a suitable solution for protecting steel pipes from erosion-initiated damage is of great important [11–14]. Nickel based coatings are providing an alternative to various challenges due to the ease of tailoring bath, economical fabrication, and better results. Among various nickel based like Ni-Co, Ni-W and Ni-B coatings, NiP coatings have proven to be corrosion resistant with appreciable mechanical properties in the literature [15–21]. Further enhancement of NiP coatings are carried out by synthesizing composite coating or utilizing the formation of ternary and quaternary alloy coatings. Introducing an inert and hard nano-reinforcement in chemical bath during the deposition process has led to the formation of composite coating with superior properties than the usual NiP coating. Many reinforcements have been investigated in the past to enhance the properties of NiP coatings, but ZrO$_2$ has been reported by many researchers to have better corrosion results and superior mechanical properties [22–24]. Nickel based coatings are reported to be fabricated through different routes, among various coatings synthesis techniques, electroless, dc electrodeposition and pulse

---

* Corresponding author at: Center for Advanced Materials, Qatar University, Doha, 2713, Qatar.
E-mail address: shakoor@qu.edu.qa (R.A. Shakoor).
[1] Authors with equal contributions.

electrodeposition are grabbing substantial attention due to their simpler experiment design and product output. For instance, electroless deposition is known for its uniformity, durability and versatility in substrate selection but has limited bath life, higher operating temperature for longer duration making it time and heat intensive process resulting in increasing the cost [25–27]. However, electrodeposition has controllable completion rate, inexpensive equipment and higher bath stability but lacks uniformity on the coat and restricted to only conductive substrate options. Pulse electrodeposition has further advantages of smooth and fine grain deposition along with more parameters to be optimized making the process complicated. All the techniques have some advantages and disadvantages over other counterparts making is complicated for their use in specific application [28]. Advances in production and characterization of nanoparticles led to innovative findings across many industries. Reinforcing the nanoparticles in NiP matrix has been investigated in the recent years and is reported to possess amazing properties due to the formation of nanocomposite coatings some of the examples of reinforcements are TiC, AlN, Y_2O_3, TiN, Al_2O_3, TaC, SiC, MoO, ZnO, CeO_2, TiO_2 and PTFE etc. [29–36]. Moreover, reinforcing zirconium oxide has been reported to appreciably improve corrosion resistance and mechanical properties of NiP based nanocomposite coatings [24,37]. Most of the previous studies have been carried out by employing electroless method for the fabrication of NiP-ZrO$_2$ composite coatings. However, our previous study that utilized the pulse-electrodeposition technique to prepare NiP-ZrO$_2$ nanocomposite coatings that reported best corrosion results and mechanical hardness for different adding content of ZrO$_2$ nanoparticles in the chemical bath. It will be quite interesting and feasible to explore the impact of various deposition techniques on the erosion behavior of NiP-ZrO$_2$ nanocomposite coatings having the same composition. In the current study, we have synthesized NiP-ZrO$_2$ nanocomposite coating through electroless deposition, electrodeposition and pulse electrodeposition techniques with constant concentration of 1 g/L of ZrO$_2$ in the chemical bath based on our last study in all the deposition. Moreover, its exhaustive erosion testing is carried out through at various angles, speeds and time to investigate the effect of erosion on nanocomposite coating and to elucidate the best fabrication route for nanocomposite coatings.

2. Methods and techniques

2.1. Materials

The chemical bath for electroless deposition was prepared by utilizing a standard commercial-grade Nichem 3010 (A and B) solutions obtained from Atotech Inc., Berlin, Germany; with nickel sulfate (Ni_2SO_4) as the Ni source, and sodium hypophosphite ($NaPO_2H_2$) as the reducing agent and as a P source [38]. However, the chemical bath for electrodeposition and pulse electrodeposition was prepared in the laboratory that contained nickel sulphate, nickel chloride, sodium chloride, orthophosphoric acid, sodium hypophosphite and boric acid purchased from Sigma Aldrich. Zirconium oxide powder with particle size ranging between 15 and 25 nm were obtained from Alfa Aesar. Other chemicals for activations, sonication and pretreatments were also purchased from reputed suppliers. Nickel sheet and mild steel substrate were procured from local suppliers.

2.2. Methodology

An electroless chemical bath was prepared by thoroughly mixing Nichem A, Nichem B and deionized water. The manufacturer provided the specific concentration of Nichem A and Nichem B, whereas deionized water was the balance for a liter of solution. The steel coupons were ground up to 2000 silicon carbide paper starting from 80 grit size to obtain a highly polished surface for electroless deposition. The steel substrate was subjected to the pretreatment of sonication for 30 min, alkaline bathing (3 wt% NaOH and 3 wt. % Na$_2$CO$_3$) at 60 °C for 30 min,

and acidic activation (15% HCl) for 45 s before placing it in the main chemical bath. Each pretreatment step was accompanied by rinsing the substrate thoroughly with deionized water. The chemical bath with zirconia nanoparticles of 1 g/L being stirred in the chemical bath at 300 rpm, at 90 °C. Two hours of deposition was carried out to come up with the thickness of around 20 μm. The coated sample were rinsed with distilled water, sonicated for 15 min and dried in air before storage. More details of the chemical bath and operating conditions are presented in Tables 1 and 2 Electrodeposition and pulse electrodeposition was carried out from the modified Watts bath. The steel substrate with 32 mm square shape was ground upto 1200 silicon carbide grading grit paper to obtain fairly polished surface. Sonication for 30 min and acid etching (15% HCl) was carried out before immersing it electrolytic bath. The zirconia particles were introduced in chemical bath before an hour of actual deposition and stirred at 300 rpm to restrict any agglomeration and settling of nanoparticles at the bottom of chemical bath. Nickel sheet was made as anode and pretreated substrate was made cathode to complete the circuit with entire deposition carried out at 65 °C. Current density and other factors were kept the same as per our previous study [24,39]. The deposition time was adjusted to obtain the thickness of more than 20 μm. More details of chemical bath and optimized conditions are tabulated in Tables 1 and 2.

2.3. Erosion test

An air-jet erosion tester was used to test the prepared coatings for erosion as shown in Fig. 1. Alumina (Al_2O_3) powder with particle size ranging from 53 μm to 84 μm were used as an erodent. The ASTM G76 standard was followed in the experimental setup for the erosion testing [40]. The erodent particles were fed at a rate of 0.94 g min^{-1} and ejected from the nozzle at a velocity ranging from 19 to 49 m/s. The nozzle diameter was 2 mm, and the particle speeds were calculated using the double-disc approach, as Ruff and Ives demonstrated in a concise explanation for determining the speed of particle by gas pressure adjustment [41]. The impacting distance was 10 mm between the nozzle outlet and the test specimen. The effect of the particles incident on the surface deformation and depth were investigated by mounting the sample on the holder with a different incident angles facing the nozzle for different exposure times. The erosion rate can be calculated by measuring the weight loss of the tested sample and the consumed eroding particles during the exposure test as derived in equation below [42]:

$$ER = \frac{W_{before} - W_{after}}{W_{erodent}} \tag{1}$$

A microelectronic balance with an accuracy of 0.00001 g was used to measure the samples' weight before taking them out of the dry cabinet to avoid the humidity effect. After washing, blowing, and washing in the ultrasonic bath with alcohol, samples were then dried and stored in a dry cabinet for at least two hours after the tests to ensure all sand particles are ultrasonically removed as well as differential humidity is not a factor.

Additionally, the erosion depth and surface roughness measurements for the tested samples were elucidated using a 3D-optical surface metrology system of Lecia DCM8 profilometer. Table 3 demonstrate the

Table 1
Chemical composition of the different deposition baths.

Chemical Bath	Pulse	Electrodeposition	Electroless
Nichem 3010 A	NIL	NIL	57 ml
Nichem 3010 B	NIL	NIL	126 ml
Nickel Sulfate hexahydrate	250 g/L	250 g/L	NIL
Nickel Chloride hexahydrate	15 g/L	15 g/L	NIL
Boric acid	30 g/L	30 g/L	NIL
Sodium Chloride	15 g/L	15 g/L	NIL
Phosphoric acid	6 g/L	6 g/L	NIL
Sodium Hypophosphite	20 g/L	20 g/L	NIL
ZrO$_2$ concentration	1 g/L	1 g/L	1 g/L

Table 2
operating condition of the different deposition baths.

Operating conditions	Pulse	Electrodeposition	Electroless
pH	2.2 ± 0.2	2.2 ± 0.2	4.0 ± 0.2
Bath temperature	64 ± 2°C	64 ± 2°C	90 ± 2°C
Deposition time	30 min	30 min	120 min
Current density	NIL	50 mA cm^{-2}	NIL
Peak Current density	50 mA cm^{-2}	NIL	NIL
Duty Cycle, On-Off time	50%, 5 s, 5 s	NIL	NIL
Bath agitation	300 rpm	300 rpm	300 rpm
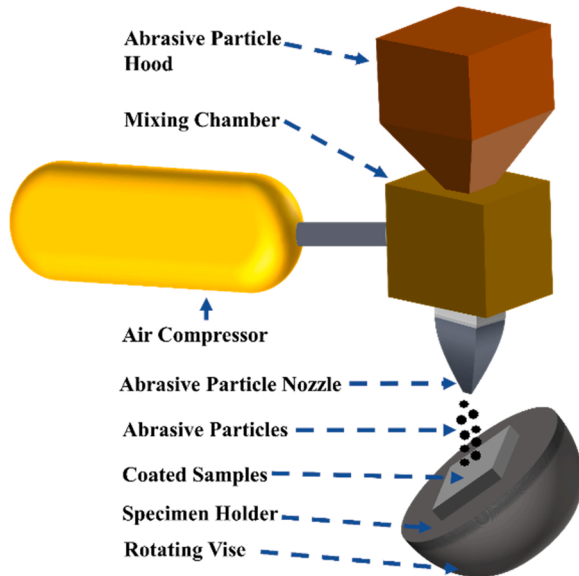
Fig. 1. Schematic diagram for the erosion tester.

erosion parameters of samples at various testing times, impact angles and particles speeds.

2.4. Characterization

X-ray diffractometer (Rigaku. Miniflex2 Desktop, Tokyo, Japan) utilizing Cu Kα radiations with the scan rate of 0.02° in the range of 2θ from 10° to 90° was used to investigate structural properties of coatings. The chemical composition of the NiP-ZrO$_2$ nanocomposite coating was determined by X-ray fluorescence spectroscopy using Energy-Dispersive X-ray Fluorescence (EDXRF) S2 PUMA model by Bruker (Karlsruhe, Germany). Field-emission scanning electron microscope (FE-SEM-Nova Nano-450, Netherlands) was employed to study the microstructural details of the coatings. Atomic force microscopy (AFM-USA) device MFP-3D Asylum research (USA) was for used for topographical survey of the coatings. The equipment contains a silicon probe (Al reflex coated Veeco model-OLTESPA, Olympus; spring constant: 2 Nm^{-1}, resonant frequency: 70 kHz) was used in these tests. All AFM investigations were performed at room temperature using tapping mode in the air. Vickers Microhardness tester (FM-ARS9000, USA) and MFP-3D Nanoindenter coupled with AFM were deployed to explore the mechanical properties of the coated samples. Microhardness measurement took place at 25 gf and 10-second dwell time. Berkovich diamond indenter tip with

Table 3
Erosion test parameters.

Erodent particles	
Velocity	19, 34, 41 and 49 m/s
Impact angle	45°, 60°, 75° and 90°
Nozzle diameter	2.0 mm
Sample-nozzle distance	20.0 mm
Test time	60, 120, 240, 480 s

maximum 1mN indentation force was installed to evaluate the nano-indentation behavior of the coatings.

3. Results and discussion

3.1. Coatings surface characterization

Fig. 2 shows XRD diffractogram of as-plated NiP-ZrO$_2$ nano-composite coatings which was synthesized through electrodeposition, electroless and pulse-electrodeposition techniques. All the spectra reveal an amorphous behavior of nanocomposite coating with a broad peak of Ni (111) at around 2θ of 44° which can be attributed to the face centered cubic lattice structure of nickel. Moreover, amorphous structure can be ascribed to the lattice distortion caused by the phosphorus atom during the co-deposition process. Moreover, heterogeneous nucleation sites provided by ZONPs during the deposition can also contribute to the inhibition of crystal growth of Ni and hence forming a complete amor-phous structure of the nanocomposite coating. Presence of ZONPs can be clearly observed from the sharps peaks at 28.2° and 31.4° attributing to ZrO$_2$(−111) and ZrO$_2$(111) in the samples prepared through various techniques. Low intensity peaks of ceramic nanoparticles in electro-deposited sample can be due to the shielding provides by the broad amorphous NiP matrix. Moreover, short peak of Fe (211) can be observed in diffractogram at 82.4° for the carbon steel substrate. These observations are in line with the literature [24,43]. The X-ray fluores-cence (XRF) analysis was utilized to detect the Ni, P, Zr and Fe content on the metal substrate. Table 4 represent the elemental analysis for NiP-ZrO$_2$ coatings that are synthesized by different deposition tech-niques. The results shows the domination of nickel content despite reducing 4% in electroless deposition technique. Meanwhile the P con-tent increase more than 2% electroless deposition technique compared to the other deposition methods. Additionally, the Zr content is the lowest with 0.8 % in the coating matrix of electrodeposition technique. It is worthy mention that increasing the phosphorous content would increasre the brittlness of the coating matrix [24,39].

Fig. 3 provides clear comparisons of the roughness profiles of NiP-ZrO$_2$ nanocomposite coatings that are synthesized by different deposi-tion techniques. The average roughness (R_a) of the coating prepared by pulse method is 11.9 nm and it increases to 17.6 nm and 29.8 nm for the as-prepared coatings by electrodeposition and electroless technique, respectively. It has been reported previously that the addition of 1.0 ZrO$_2$ nanoparticles increased the grain growth and surface roughness of the coatings which attributed mainly to the presence of ceramic species into the NiP matrix. Furthermore, the RMS roughness increased from 15.5 to 24.1 and 39.7 nm for the nanocomposite coatings in comparison at different deposition technique, which is consistent with the average roughness. By applying pulse method to the electrodeposition and electroless method the coating had a higher surface roughness [26,27]. Fig. 4 depicts the surface morphology and the thickness of the as-prepared NiP-ZrO$_2$ coatings using different deposition techniques. The surfaces of the NiP-ZrO$_2$ coating prepared by pulse technique contain a nodular structure with a uniform distribution of ZrO$_2$ nano-particles with a rarer microvoids, which was explained in previous work [34]. Meanwhile, fewer nanoparticles were present on the NiP-ZrO$_2$ coating prepared by the electrodeposition technique. Additionally, the microvoids on the NiP-ZrO$_2$ coating prepared by the pulse technique was less than that on the electroless technique with a noticeable loosely metallic particle, and ZrO$_2$ nanoparticles agglomeration. This result indicates that the NiP-ZrO$_2$ coating prepared by the pulse deposition technique is dense [22]. Surface grain size of the coating is nanometer-sized, resulting in a dense and smooth appearance, with a few micron-sized wrinkles and dispersed particles. A cross-sectional SEM image of NiP-ZrO$_2$ coating with an average thickness of around 20 μm is shown in Fig. 4. There may be a difference in the distribution of metal particles on the surface of coatings, which may affect erosion resistance.
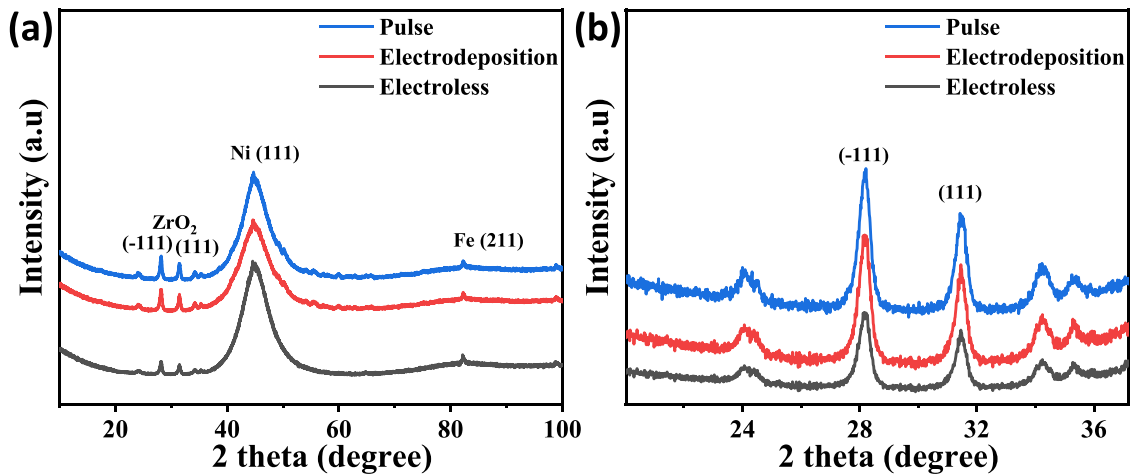
Fig. 2. XRD spectra for NiP-ZrO$_2$ synthesized through different deposition techniques.

Table 4

XRF analysis for NiP-ZrO2 coating prepared by different techniques.

	Ni	P	Zr	Fe
Pulse	87.2	9.8	1.7	1.1
Electrodeposition	87.9	9.9	1.1	0.8
Electroless	83.9	12.6	1.8	1.5

3.2. Mechanical properties

Measurement of Vickers hardness of the NiP-ZrO$_2$ nanocomposite coatings fabricated through different techniques was performed with a MicroMet micro-indentation tester. The hardness of each surface was measured by forcing an indenter into the surface for ten seconds with a 25-gram. five hardness measurements were taken for each specimen, and an average result was calculated. Vickers hardness is calculated using equation below

$$HV = \frac{1.8544 * F}{d^2} \tag{2}$$

where F equal to the force applied to the indent in kilograms-force, and d equal to the average distance of the indent in millimeters.

As presented in Fig. 5, microhardness of the pulse samples are in the range of 600 HV$_{25}$ to 700 HV$_{25}$. Electrodeposition samples exhibit slightly lower range than pulse samples with the range of 500 HV$_{25}$ to 630 HV$_{25}$. Moreover, microhardness values of electroless nanocomposite coatings lie in the range of 560 HV$_{25}$ to 590 HV$_{25}$. The improvement in the microhardness can be attributed to dispersion hardening and Hall-Petch effect [44,45]. Additionally, the nano-indentation depth of samples is shown in Fig. 5. The hardness relates to the microstructure and phase compositions of coatings. The indentation depth of the electroless sample was about 212 nm. Moreover, for the conventional electrodeposition, the maximum indentation depth obtained is nearly 200 nm. In case of pulse electrodeposition, the
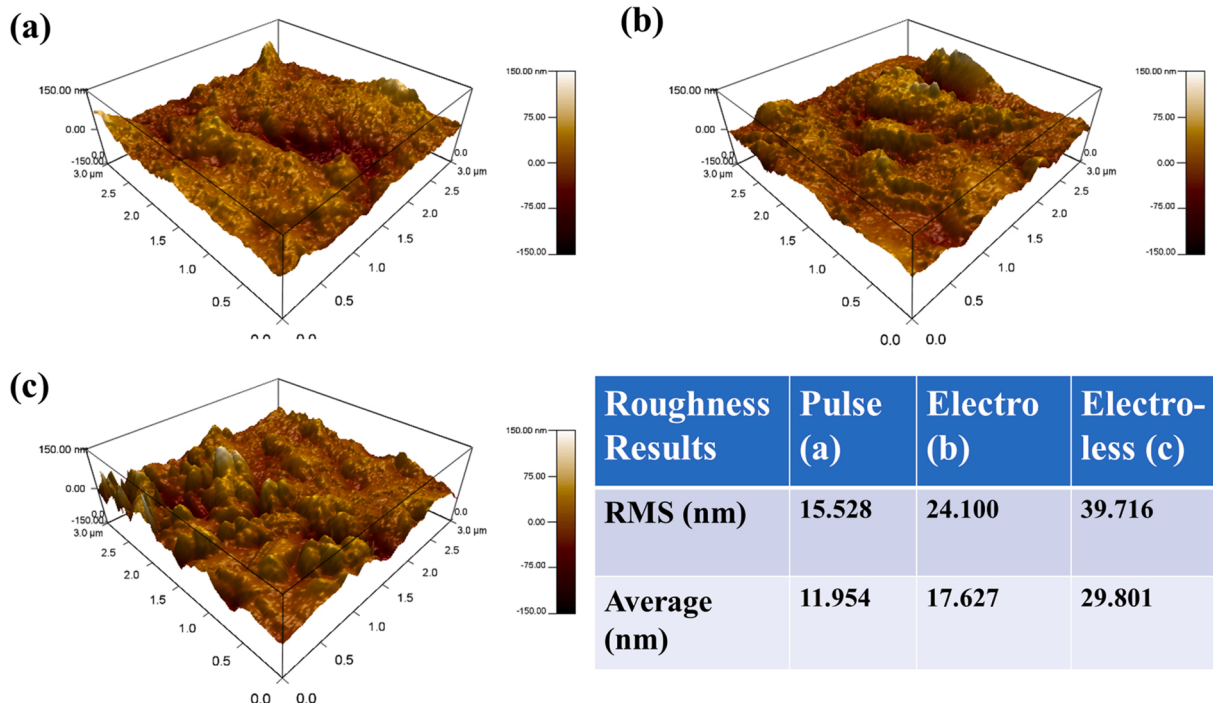

Roughness Results	Pulse (a)	Electro (b)	Electro-less (c)
RMS (nm)	15.528	24.100	39.716
Average (nm)	11.954	17.627	29.801

Fig. 3. AFM surface topography for the as-prepared NiP-ZrO$_2$ coatings using different deposition techniques (a) pulse, (b) electrodeposition and (c) electroless.
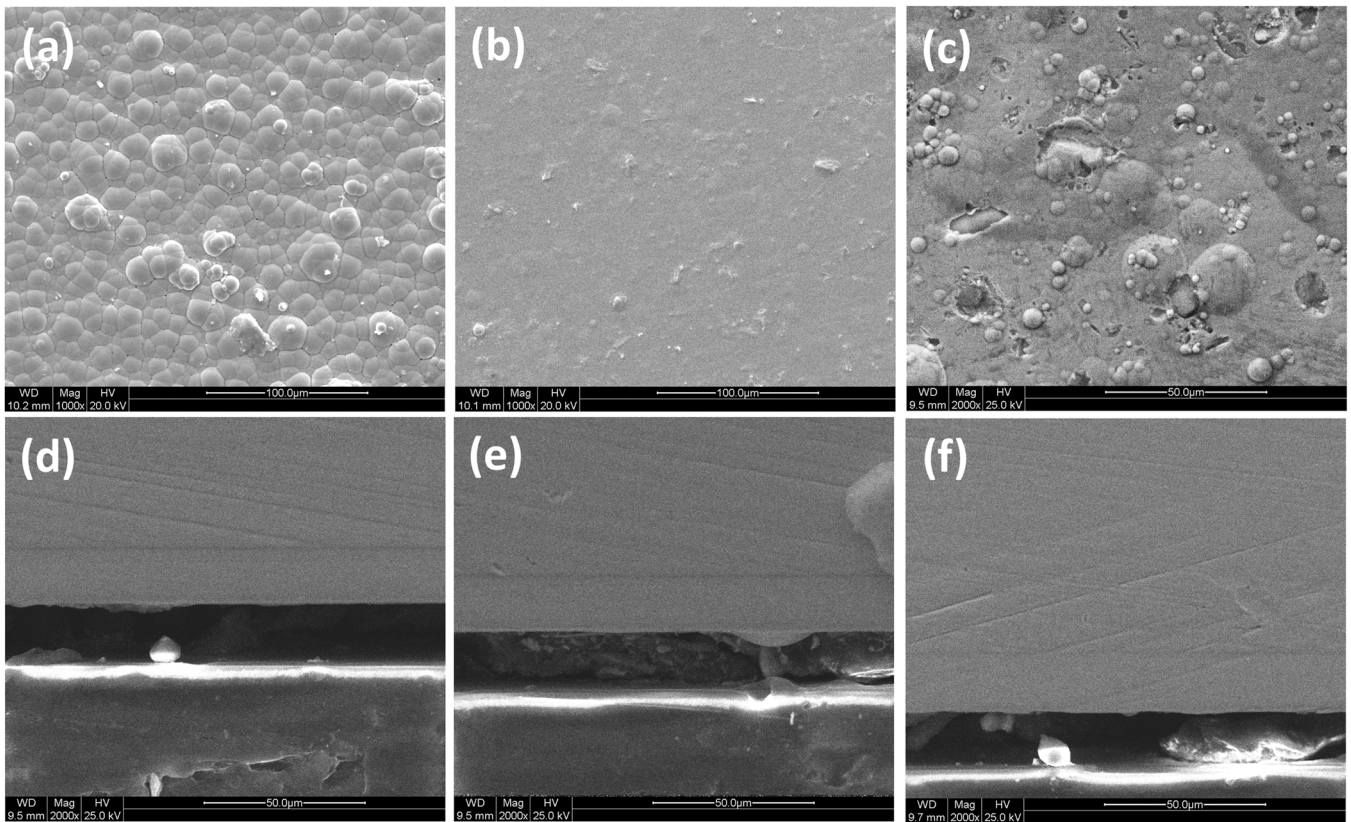
Fig. 4. SEM surface topography and cross sectional images for NiP-ZrO$_2$ coating prepared by different techniques (a, d) pulse, (b, e) electrodeposition and (c, f) electroless.
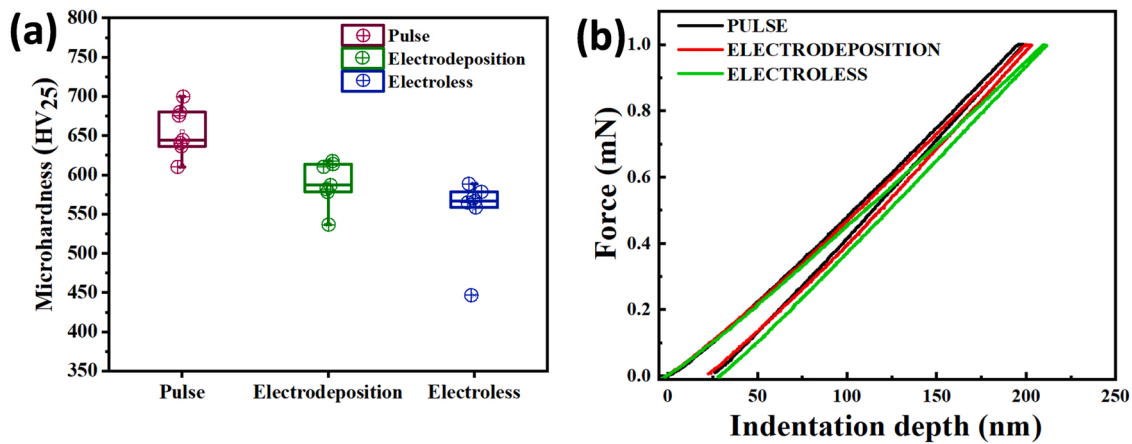

Fig. 5. (a) Viker microhardness and (b) Nanoindentation curves for the as-prepared NiP-ZrO$_2$ coatings using different deposition techniques.

indentation depth of the coating was improved to 190 nm for the sufficient distribution of ZrO$_2$ particles in the coatings. The increase in hardness may be attributed to the dispersion hardening and microstructural enhancement of the deposition [46–48]. The high hardness can enhance the erosion performance of the fabricated coatings.

3.3. Gravimetric analysis and erosion resistance of the different coatings

Fig. 6 depict the effect of test duration, impact angle and particles velocity on the mass loss of NiP-ZrO$_2$ nanocomposite coatings by different deposition techniques. Fig. 6(a) shows the weight loss of the as-deposited NiP-ZrO$_2$ coatings by different deposition techniques versus time. Specimens were eroded using a velocity of 34 m/s for 60, 120, 240 and 480 s at 90° impact angle. It can be noticed that the weight loss

measurements for the different NiP-ZrO$_2$ coatings at different exposure time show a similar trend and the as-synthesized coatings by electroless techniques is higher than other deposition techniques. Additionally, it is evident that the weight loss values gradually drop with increasing time which can attributed to interacting the substrate to the erodent particles. The results of the erosion test in Table 5 with respect to different exposure time, impact angles, and particle velocity. It can be noticed for a short period of exposure the erosion rate is seemed to be similar for the pulse and electrodeposition techniques. However, the erosion rate for the electrodeposited coating became higher than the pulse deposited coating with increasing time. It is worthy mentioning that the erosion rate decreases significantly at 480 s of erosion time which could be an evident for a contribution of the base material on the erosion rate results [22,49]. Intriguingly, electroless coatings have a higher erosion rate
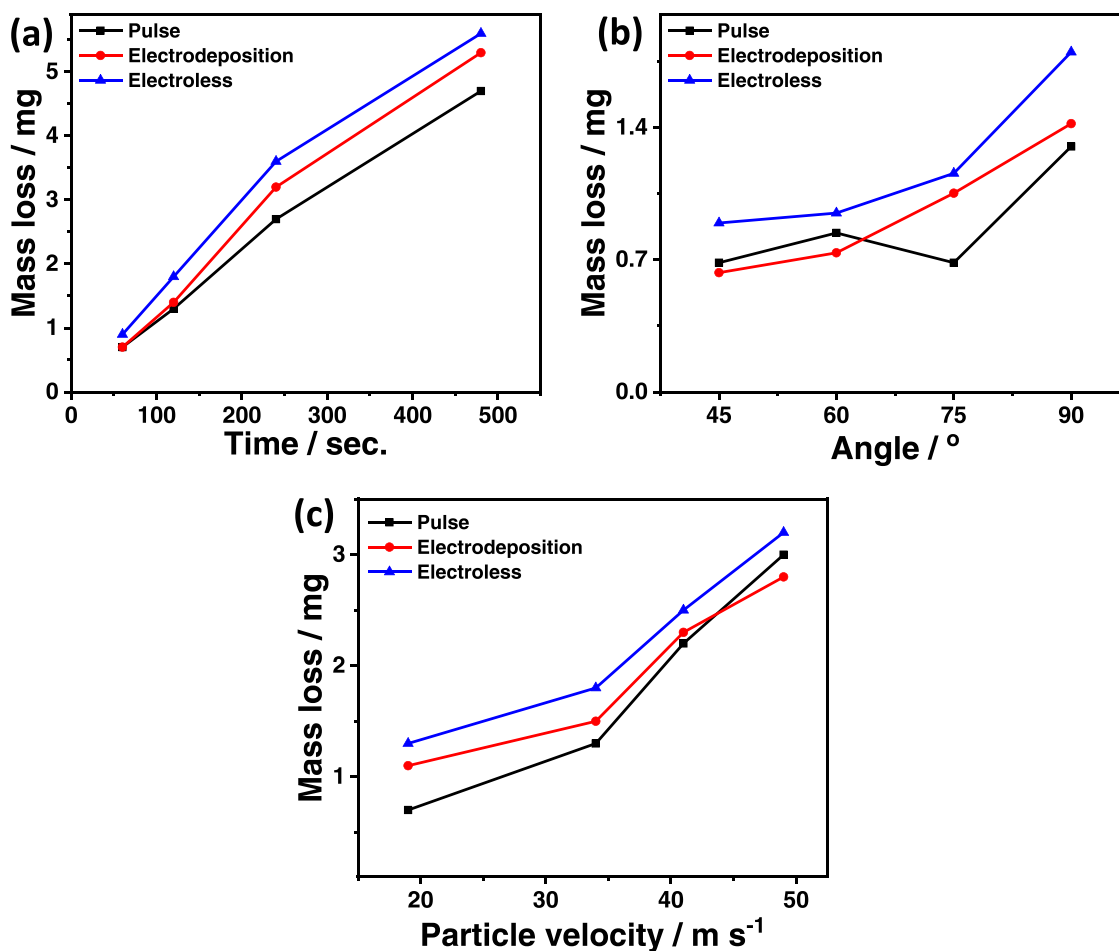
Fig. 6. Mass loss measurements of the as-deposited NiP-ZrO$_2$ nanocomposite coatings by different deposition techniques after exposure test at different a) exposure time, b) impact angles, and c) particles velocity at definite constant condition for each measurement.

than other deposition techniques. the brittleness nature of the diverse types of NiP-ZrO$_2$ coatings might explain this difference between electroless coatings and coatings synthesized by pulse and electrodeposition techniques, as discussed in the mechanical properties section [50,51]. Additionally, the effect of impact angle on mass loss was evaluated and is presented in Fig. 6(b). The as-deposited NiP-ZrO$_2$ coatings by different deposition techniques were eroded at 45°,60°,75° and 90° for 120 s. It is evident that the weight loss of electroless coated specimen significantly increases with increasing impact angle. However, weight loss of pulse deposition coating is slightly higher at angle of 60° and drops with increasing angle to 75° then it remarkably increases at 90°. The mass

loss behavior of electrodeposited coated samples is consistent with increasing the impact angle, which shows that at a relatively low particle velocity, the amount of erosion at low angle is slightly higher than 90° impact angle [52,53]. As a result of brittleness and ductility coatings merits, the incident particles are impacted on the sample surface and, naturally, their impact force is increased [47]. Therefore, the erosion rate for angles ranging from 45° to 90° is boosted for the different metallic coatings as seen in Table 5. These findings are consistent with other observations about materials ductility in microhardness and nanoindentation. There was low erosion at the lower 45° angle, which could be attributed to fewer impacting particles on the surface of the sample. Erosion rates increased with increasing impact angle primarily because of cutting/ploughing actions. The erosion rate was greatest at approximately 90°, where most of the particles were involved in removing the material and the interference between the incoming particles and the rebounding particles was minimal [28]. It has been reported previously that the erosion rate is affected by the impact angle as it depends on the ductility of the material. Materials with a high erosion rate at low incident angle are ductile while, the erosion rate of the brittle materials are the maximum at or near 90°. For ductile material at low impact angle, ploughing and cutting actions are the most dominate influences, and this results in high erosion. meanwhile, brittle materials fracture and high material loss at high impact angle, whereas ductile materials experience heavy plastic deformation. Fig. 6(c) present the influence of the particles velocity on the weight loss measurements of the different types of NiP-ZrO$_2$ nanocomposite coatings. Generally, the mass loss of the different coatings increases with increasing particle velocity. Previous studies have confirmed that higher particle motion

Table 5
Normalized erosion rate values of the as-deposited NiP-ZrO$_2$ nanocomposite coatings by different deposition techniques under different influences exposure time, impact angle and particle velocity.

		Pulse	Electrodeposition	Electroless
Time (sec.)	60	0.25	0.26	0.31
	120	0.28	0.28	0.33
	240	0.30	0.33	0.35
	480	0.31	0.34	0.35
Angle (°)	45	0.18	0.16	0.21
	60	0.20	0.18	0.23
	75	0.17	0.23	0.26
	90	0.27	0.28	0.34
velocity (m/s)	19	0.21	0.30	0.34
	34	0.27	0.3	0.33
	41	0.30	0.31	0.33
	49	0.30	0.28	0.31

results in more significant removal of material from the surface [54]. This could be attributed to higher particle velocity being associated with higher kinetic energy, leading to more material removal. interestingly, the brittleness and ductility coatings merits of the different coatings are less noticeable at higher velocities than lower ones. Moreover, the erosion rate in electroless deposited samples appears to increase with jet velocity acceleration. It is worthy mentioning that the erosion rate is directly proportional to speed of the particles as shown in Table 5. The erosion rate of pulse deposited coatings was lower than that of electrodeposited and electroless coatings, respectively.

3.4. Surface erosion topography

The erosion rate data has been verified by numerous characterization studies that provide a better understanding of erosion features [55,56]. Profilometric scans were performed on a different types of coating specimens after 120 s of erosion time at 90° of incidence angle for different particles impinging speeds. Scanned profiles were stitched together for comparison as shown in Fig. 7. The 3D erosion scars of attack vary from 5 mm to 7 mm for 19 and 49 m/s particles velocity, respectively. The as-deposited electroless deposited coating exhibits pile-up at both low and high velocities, whereas no obvious pile-up is observed on the as-deposited pulse or electrodeposited coatings after the impact testing as seen Fig. 7. This indicates that the pulse deposited coating is more ductile than the electrodeposited and electroless coatings. Fig. 8 shows the surface erosion profiles of samples at various impact angles. When the impact angle is altered from 45° to 90°, erosion scars had developed from narrow grooves to deep round holes. During a 90° impact angle, the eroded region is circular, with a noticeable pile up for electroless deposited coating. Meanwhile at a 45° impact angle, the eroded scare takes an elliptical shape with apparently microcracks

joined with the coating pile up. The size of the erosion scar along with the longitudinal and the lateral direction are approximately 5.67, 6.47 and 8.31 mm^2, for 45° angle of incidence and 34 m/s velocity for pulse, electrodeposited and electroless coatings, respectively. three distinct zones can be clearly observed in the eroded pulse and electrodeposited coating specimens; the central zone is where most material was eroded, the second zone is where less material was consumed, and the third zone represents the least amount of erosion as shown in schematic diagram (Fig. 12). However, the erosion tracks of coating began to show coating removal, which is mainly related to the looseness and micro-cracks of the electroless coating specimen.

3.5. Crater depth and surface roughness measurements

The maximum crater depth and the estimated surface roughness of each coating sample is presented in Fig. 9. This was done because higher values of depth of cut may lead to increased component failure risk. The findings of maximum depths of cut were summarized to depict the effect of exposure time, impact angle and particles velocity, respectively. Additionally, the surface roughness is an interpretation of erodent emphasizes that surfaces with a rough surface would wear more quickly and have higher depth than smooth surfaces. it is worthy mentioning that the surface roughness is derived from the following equation: [28].

$$Ra = \iint a \lfloor Z(x, \quad y) \rfloor \quad dx \quad dy \tag{3}$$

Ra represents the average roughness, "a" implies that the calculation is performed on the area measured, Z is the distance from the deepest point in the damaged zone to the unaffected surface of the specimen, and (x,y) represents the height in relation to the measured area. Fig. 9(a) shows the depth of the erosion tracks on the different NiP-ZrO$_2$
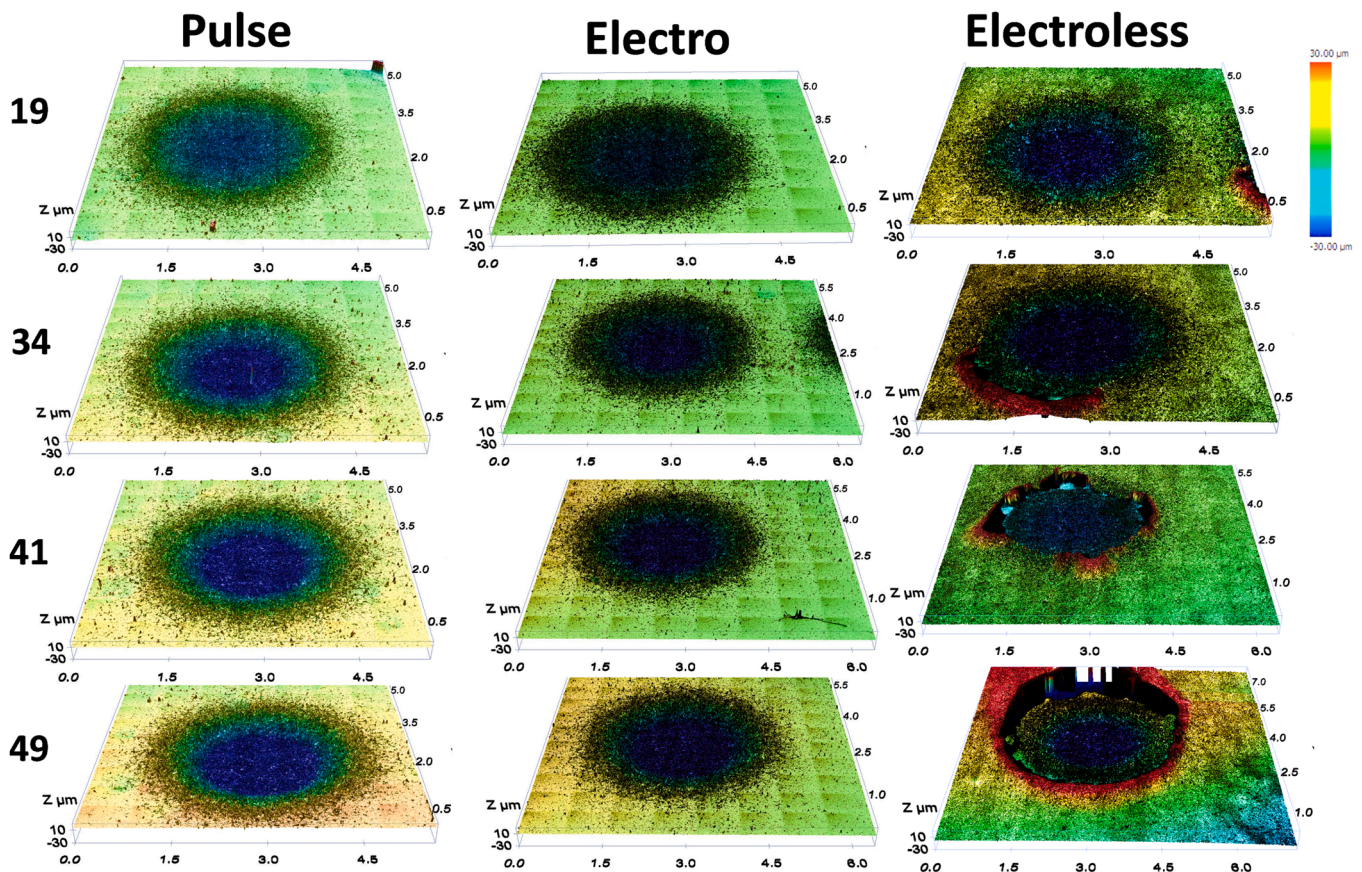

Fig. 7. 3D surface profilometer of the as-prepared NiP-ZrO$_2$ coating by different deposition technique after erodent impacted for 120 s and 90° with different erodent velocity.
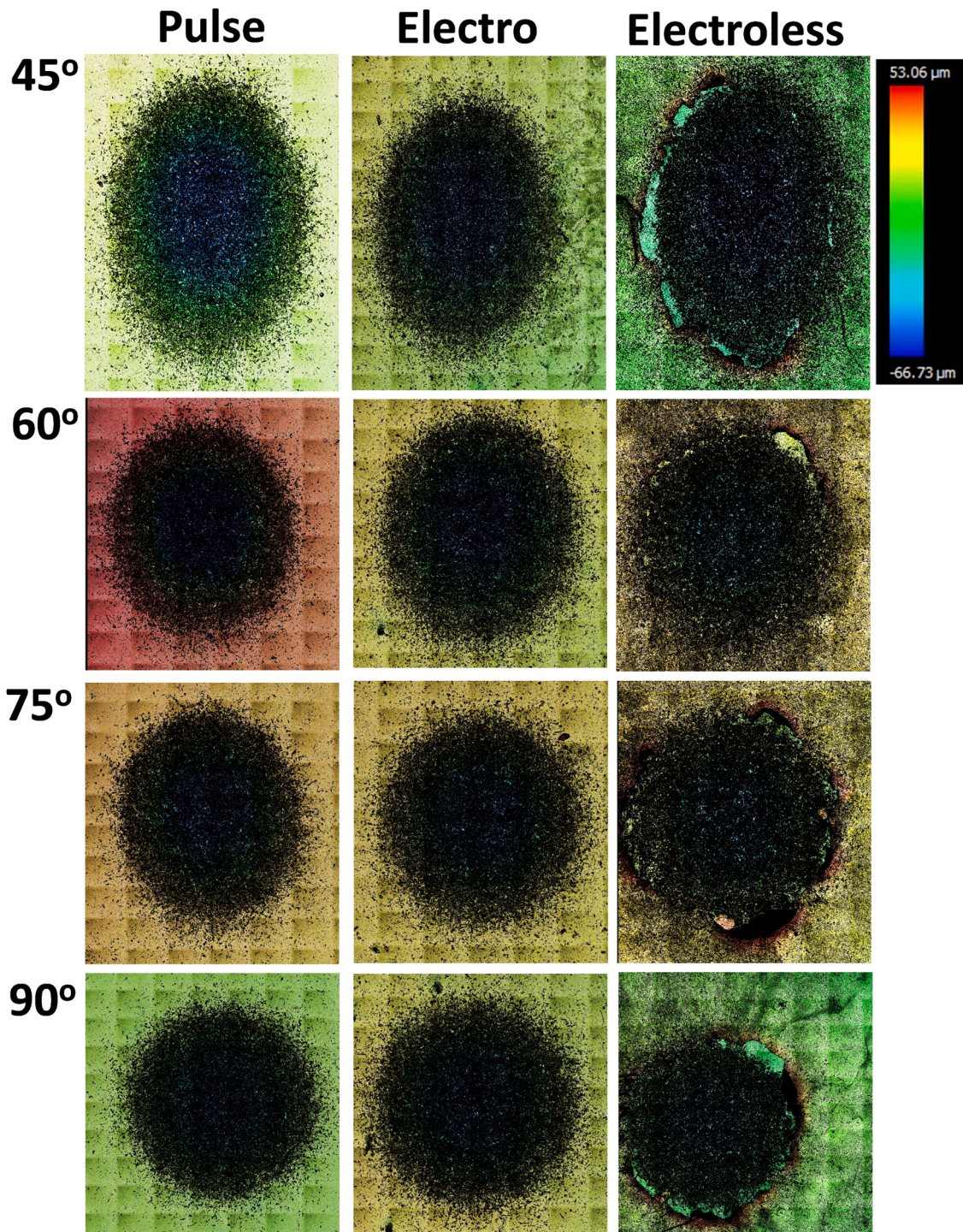
Fig. 8. 2D surface profilometer for the as-prepared NiP-ZrO$_2$ coating by different deposition technique after erodent impacted for 120 s and 34 m/s with different angle.

deposited coatings after different exposure time of erosion at 90° and 34 m/s of particles impinging velocities. It can be noticed that the crater depth at electroless coating is two times higher than the measured depth in pulse deposited coating after 60 s of erosion time. Meanwhile, with increasing the exposure time the change in depth measurements decreases reaching to the lowest difference after 240 s of erosion. It indicates that the erosion depth of the pulse deposited coating was much diminisher than the electroless coating. It is believed that the surface characteristics and high hardness of the coating contribute to the good erosion resistance of pulse deposited coatings. Similarly, increasing the

coating hardness would reduce its deformation susceptibility during erosion test. Intriguingly, the correlation between the surface roughness and the testing time shows a proportionally increases in surface roughness with longer testing times reaching to 289 μm in electroless coating after 480 s of exposure. This indicates the deterioration of the surface due to erosion after prolonged use as can be seen in Fig. 9(b).

Fig. 9(c) shows the influence of the impingement angles 45°, 60°, 75°, and 90° on crater depth. Comparing the different NiP-ZrO$_2$ coating samples, the erosion depth of electroless coating was higher than the erosion depth of electrodeposited and pulse deposited samples.
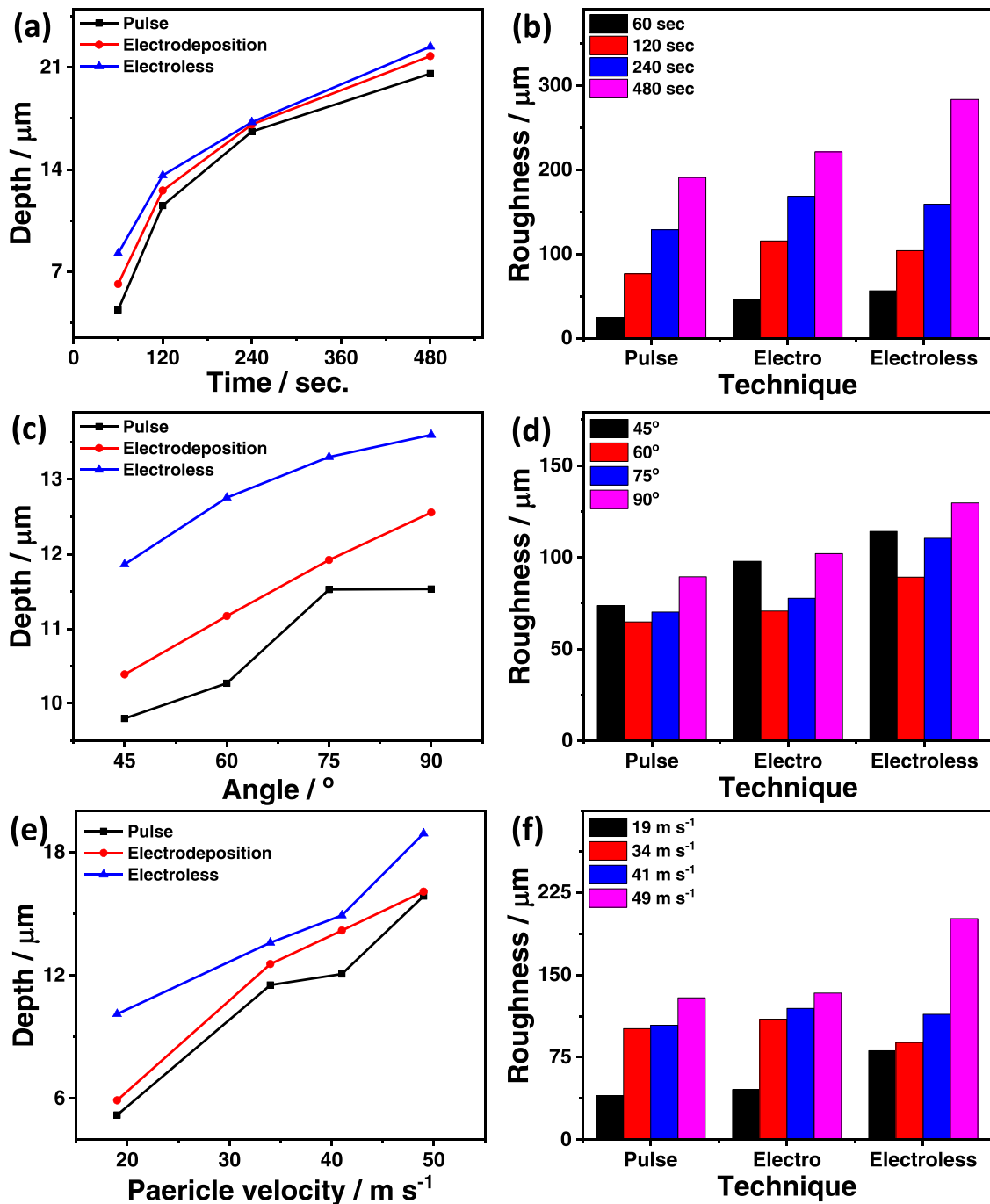
Fig. 9. surface roughness measurements of the as-deposited coatings by different deposition techniques after exposure test at different a) exposure time, b) impact angles, and c) particles velocity at definite constant condition for each measurement.

Moreover, pit depths at 90° were higher than those at 45° in the different coatings. It is worthy mentioning that in pulse deposition coating, as the angle increases to 75°, craters elongate and become deeper resulting in steep increase in erosion depth. However, at 90° impact angle, the craters continue to extend but have become shallower thereby resulting in erosion depth similar to 75° impact angle. In contrast, the results of the roughness in Fig. 9(d) for the different NiP-ZrO$_2$ coatings after impingent with altering impact angles are progressively decreased after exceeding the particles impact angle to 60°. The roughness dropdown is varied from coating to another based on its mechanical properties. Then, with varying impact angles, the results are similar to the erosion rate and depth of cut results.

Fig. 9(e) shows the maximum measured depth as a function of particle speed at 120 s of exposure time and 90° of impact angle. Depth is proportional to particle velocity, indicating higher coating loss as speed increases. Additionally, the maximum erosion depth at 49 m/s has been reduced from 18.9 to 15.8 μm which converting the deposition technique from electroless to pulse deposition technique.

Fig. 9(f) shows the surface roughness measurements with altering the particles velocity. It can be noticed that the roughness assessed around three times of increase for the different coatings as it shifts from 40.1, 45.3, 101.5 μm at 19 m/s to 129, 133, 201.2 μm at 49 m/s for pulse, electrodeposited and electroless coatings, respectively.

3.6. SEM analysis

Figs. 10 and 11 depict the surface morphology and cross section images for the different as-synthesized NiP-ZrO₂ coatings under different particles velocity, impact angles and exposure time. Generally, the surface morphology of the eroded surfaces would be influenced by these variables which could lead to different erosion mechanism. The interactions between the target metal and the impinging particles might have changed due to the changing magnitudes of momentum vectors on the target metal surface [57,58]. Fig. 10 depict the SEM analysis for the different as-synthesized NiP-ZrO₂ coatings at two different impingement velocities 34 and 49 m/s after 120 s of erosion time with 90° of impact angle. At low particles velocity, Fig. 10(a-c), the erodent particles utilized its kinetic energy for penetrating the coating layer which take the lead to coating micro-cuttings, pullout, and embedded particles in the whole different coatings. Additionally, the coating layer is flattened out from the repeatedly strike off the abrasive particles causing a vulnerable lips and plastic deformation influence. However, the eroded surfaces didn't show any platelets form on the surface which mainly caused the coating failure. Meanwhile, increasing the particles velocity to 49 m/s at 90° of impact angle led to a noticeable ploughing marks at the eroded surface for the different deposition technique as seen in Fig. 10(d-f). The ploughing marks were accompanied with lips cutting grooves which can attributed to the repeated impact of the embedded particles with the incoming particles stream [52,55]. Commonly, the higher particles velocity, the more material removal and the deeper of abrasive particles through the coating layer. This layer became more brittle in nature and may not be removed immediately but would easily be removed by subsequent impacts by another particle. It can be observed that the erosion mechanism resulting from the higher particles velocity characterized by detachment splats, craters, random micro-cutting and a ploughing action with lips cutting grooves [59,60].

Fig. 11 shows the cross-sectional images after 120 s of erosion time on the NiP-ZrO₂ pulse deposited coating at different impact angle (45°, 60°, 75°, 90°), at 34 m/s of particles velocity. At low impact angle, the impinging particles stream propagate to deform the coating layer by a complete removal of large fragments causing a coating fracture with the presence of embedded particles of the deformed layer, Fig. 11(a). Intriguingly, a noticeable trough shape was produced with some erodent debris inside the coating layer at 60° of the impact angle. Additionally, the ploughing effect is extensively considered in removing the coating layer, hence the kinetic energy of the impacting particles is concentrated in the plastic deformation of coating layer as seen in Fig. 11(b) [47,61]. Meanwhile, at the higher impact angles, most of the erodent kinetic energy is utilized to wear down the coating layer, triggering the dimple formation and embedded abrasive particles with the ploughing action in the coating layer. Consequently, the witnessed ridges and grooves are attributed to the sequence squeezing of the dimples which accompany with coating fractures by plastic deformation as shown in Fig. 11(c and d).

The schematic erosion mechanism for the different as-prepared NiP-ZrO₂ coatings under varied erodent variables is demonstrated in Fig. 12.

1. During the erosion test with 34 m/s and 90° impacted particles for 120 s, electroless coating shows plastic deformation, micro-cutting and pullout of the coating layer. Meanwhile, embedded particles can be noticed in electrodeposited layer. In contrary, pulse deposited coating reveals groves and ploughing in the targeted area.
2. For the erodent particles with 49 m/s and 90° for 120 s, large crater with a noticeable pile-up can be observed in electroless. However, electrodeposited coating shows plastic deformation, micro-cutting and pullout of the coating layer. Meanwhile, a detachment splats with a plastic deformation is recognized in pulse deposition coating.
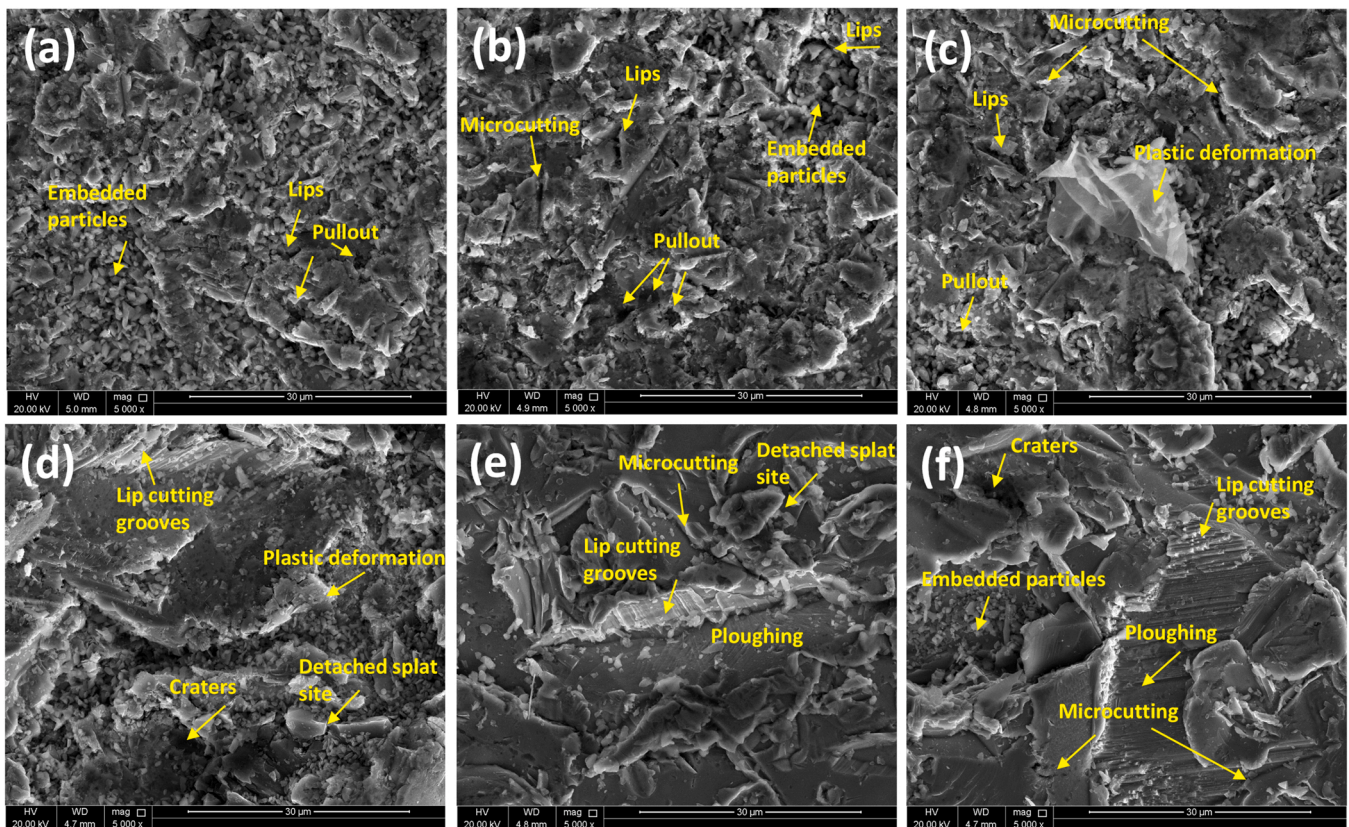

Fig. 10. SEM images for pulse (a, d), electrodeposition (b, e) and electroless (c, f) coatings after 120 s of impacted erodent with 90° at 34 and 49 m/s of particles velocity, respectively.
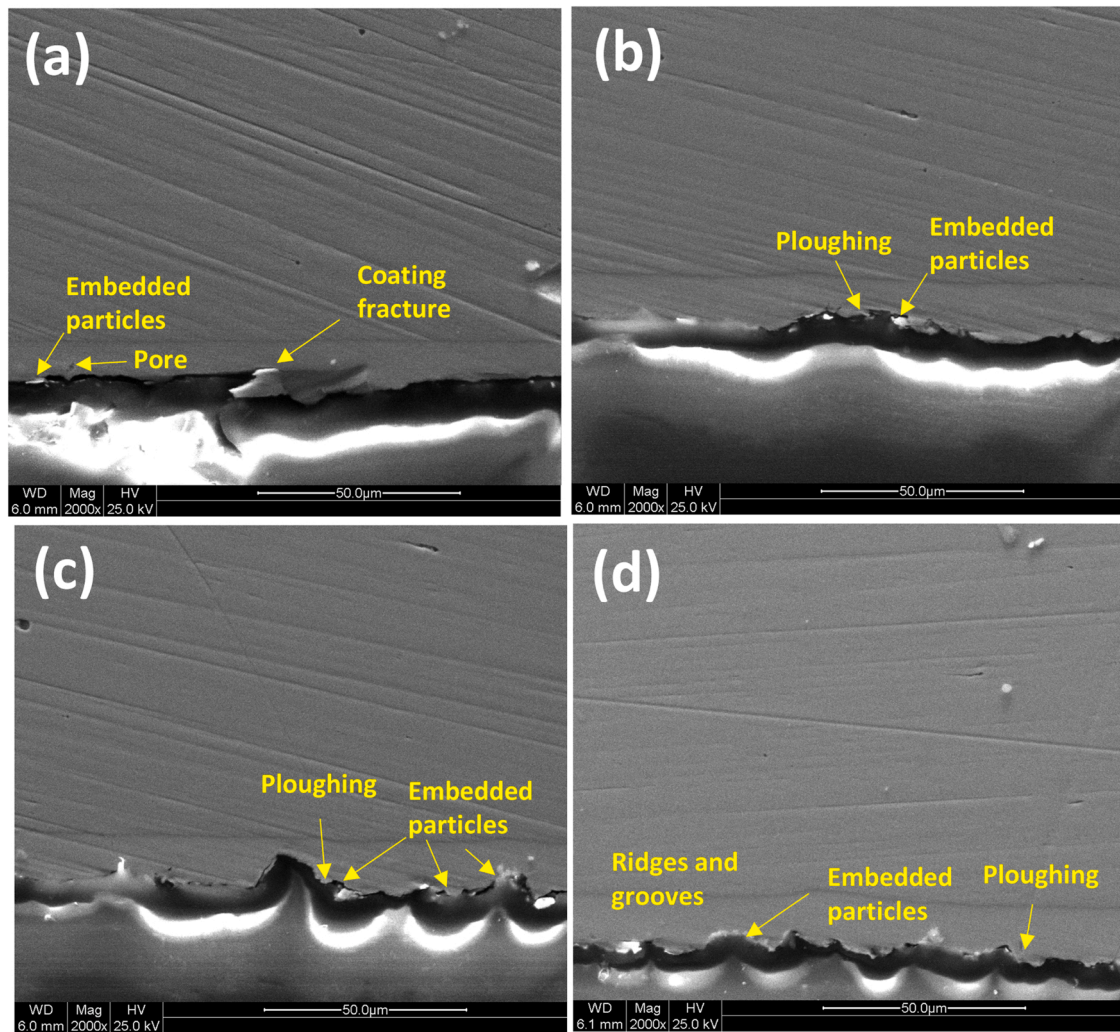
Fig. 11. Cros-sectional images for the pulse deposited as-prepared NiP-ZrO$_2$ coating after erodent impacted for 120 s and 34 m/s with different angle a) 45°, b) 60°, c) 75° and d) 90°.

3. For the erosion experiment for 480 s at 34 m/s and 90°, all coatings show the same behavior after long exposure time with plastic deformation, micro-cutting and pullout of the coating layer even reaching to the base surface in electroless coating.

4. During the erosion test with 34 m/s and 45° impacted particles for 120 s, an elliptical shape with apparently microcracks joined with the coating fracture and pullout in electroless coating. A plastic deformation with micro-cutting and the coating pullout is noticed in electrodeposited coating. Meanwhile, a plastic deformation with embedded particles and pores in the coating matrix is detected in the pulse coating layer with reducing the eroded area.

4. Conclusion

The surface and mechanical characterizations for the different as-deposited NiP-ZrO$_2$ coatings confirms that the pulse deposition technique produce a distinguish coating with an outstanding superiority in roughness, hardness, and elasticity in comparison to electroless and electrodeposition techniques. The erosion behavior of NiP-ZrO$_2$ coatings which have been synthesized by three different deposition techniques was investigated to introduce a better understanding of cutting-edge mechanism of these coatings. The influence of altering the deposition method would effect on the mechanical merits and erosion resistance of the different types of NiP-ZrO$_2$ coatings. The mass loss measurements showed a tremendous increase with increasing the exposure time and

the particle velocity due to the high kinetic energy for the erodent particles. In the meantime, the mass loss was observed to be increased with increasing the impact angle reaching to the maximum loss at the highest angular impact (90°) which indicate the brittleness of the as-synthesized coatings. However, the ductility of the NiP-ZrO$_2$ pulse deposited coating was evidently observed compared to the electroless and electrodeposited coatings. SEM images clarify the influence of the various variables in the erosion mechanism. Hence, increasing particles velocity amplified the coating deficiencies via ploughing, flattening and micro cutting of the eroded area. Meanwhile, the coating fracture is noticeable at lower impact angle compared to higher impact angle which resulted in deeper embedment of erodent particles. Additionally, the coating spallation increases with increasing the time of exposure in electroless coating. Overall, the erosion behavior of the different as-deposited NiP-ZrO$_2$ coatings are fundamentally influenced by solid particles velocity, impact angle, exposure time and the deposition technique. However, the overall erosion resistance which is driven from erosion depth, mass loss, surface roughness, and erosion rate of the as-synthesized NiP-ZrO$_2$ coating by pulse deposition technique is applicably higher than other deposition techniques.

Statement of originality

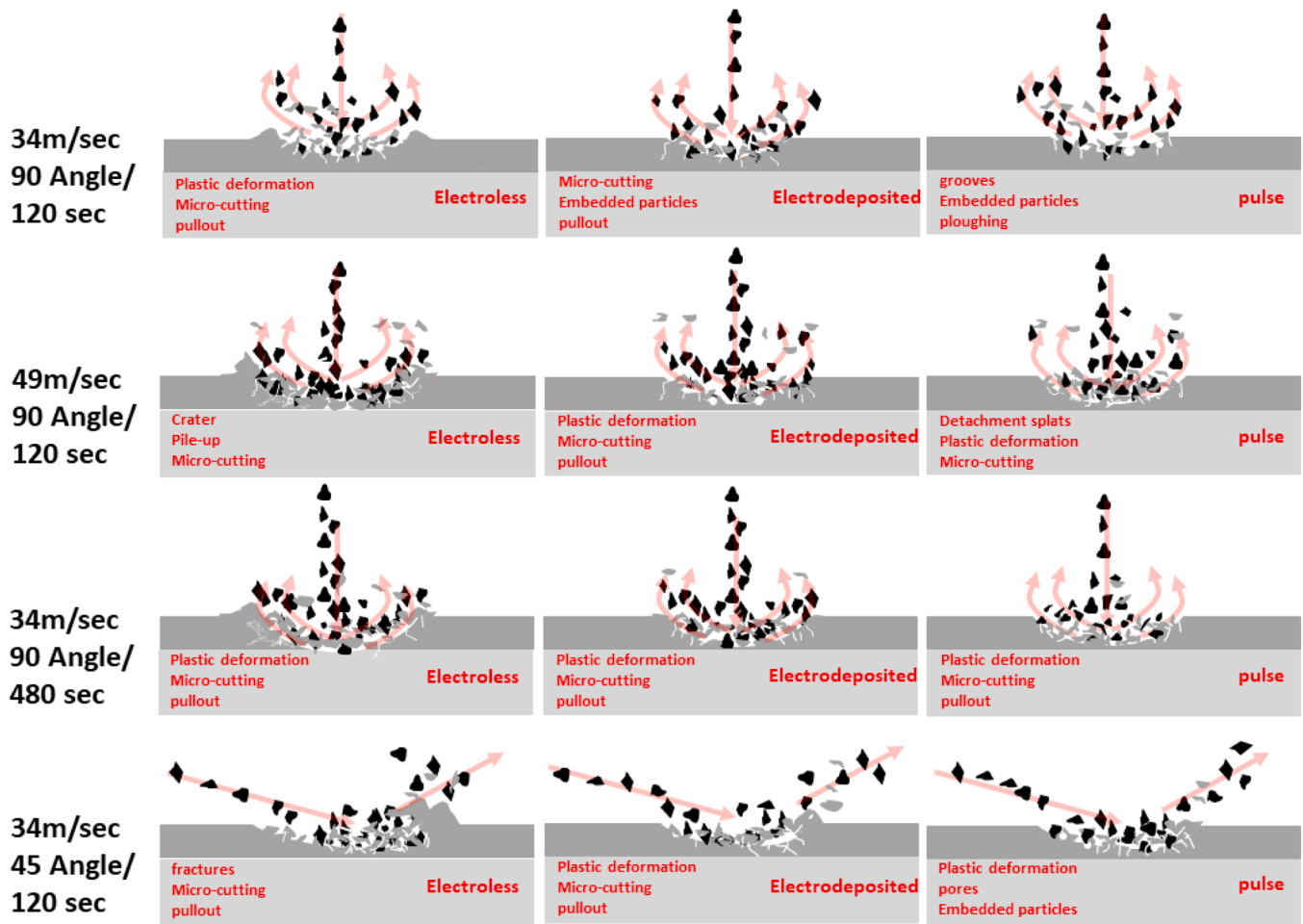As corresponding author, I **R. A. Shakoor**, hereby confirm on behalf of all authors that:

Fig. 12. Erosion mechanism of as-prepared NiP-ZrO$_2$ coatings by different deposition techniques after exposure test at different a) exposure time, b) impact angles, and c) particles velocity.

1) The paper has not been published previously, that it is not under consideration for publication elsewhere, and that if accepted it will not be published elsewhere in the same form, in English or in any other language, without the written consent of the publisher.

2) The paper does not contain material which has been published previously, by the current authors or by others, of which the source is not explicitly cited in the paper.

Declaration of Competing Interest

The authors declare that they have no known competing financial interests or personal relationships that could have appeared to influence the work reported in this paper.

Data availability

Data will be made available on request.

References

[1] Ríos-Mercado RZ, Borraz-Sánchez C. Optimization problems in natural gas transportation systems: a state-of-the-art review (https://doi.org/) Appl Energy 2015;147:536–55. https://doi.org/10.1016/j.apenergy.2015.03.017.

[2] Arabnejad H, Mansouri A, Shirazi SA, McLaury BS. Development of mechanistic erosion equation for solid particles. Wear 2015;332–333:1044–50. https://doi.org/10.1016/j.wear.2015.01.031.

[3] Yang Q, McKellar R. Nanolayered CrAlTiN and multilayered CrAlTiN-AlTiN coatings for solid particle erosion protection. Tribol Int 2015;83:12–20. https://doi.org/10.1016/j.triboint.2014.11.002.

[4] Borawski B, Singh J, Todd JA, Wolfe DE. Multi-layer coating design architecture for optimum particulate erosion resistance. Wear 2011;271:2782–92. https://doi.org/10.1016/j.wear.2011.05.035.

[5] Wood RJK. The sand erosion performance of coatings. Mater Des 1999;20:179–91. https://doi.org/10.1016/s0261-3069(99)00024-2.

[6] Fotovvati B, Namdari N, Dehghanghadikolaei A. On Coating Techniques For Surface Protection: A Review. J Manuf Mater Process 2019;3:28. https://doi.org/10.3390/jmmp3010028.

[7] Lelevic A. Ni-P coatings electroplating - A Review. Part I: Pure Ni-P Alloy 2018.

[8] Matthews S, James B. Review of thermal spray coating applications in the steel industry: part 2 - zinc pot hardware in the continuous galvanizing line. J Therm Spray Technol 2010;19:1277–86. https://doi.org/10.1007/s11666-010-9519-7.

[9] Hadavi V, Moreno CE, Papini M. Numerical and experimental analysis of particle fracture during solid particle erosion, part ii: effect of incident angle, velocity and abrasive size. Wear 2016;356–357:146–57. https://doi.org/10.1016/j.wear.2016.03.009.

[10] Hadavi V, Moreno CE, Papini M. Numerical and experimental analysis of particle fracture during solid particle erosion, part I: Modeling and experimental verification. Wear 2016;356–357:135–45. https://doi.org/10.1016/j.wear.2016.03.008.

[11] Anketell J., Learner R.C.M. Fragmentation of Shell Cases Author (s): N. F. Mott Source: Proceedings of the Royal Society of London. Series A, Mathematical and Published by: Royal Society Stable URL: ⟨https://www.jstor.org/stable/97828⟩. Proc Roy Soc A 1967;301:355–61.

[12] Wolfe DE, Gabriel BM, Reedy MW. Nanolayer (Ti,Cr)N coatings for hard particle erosion resistance. Surf Coat Technol 2011;205:4569–76. https://doi.org/10.1016/j.surfcoat.2011.03.121.

[13] Dallaire S. Hard arc-sprayed coating with enhanced erosion and abrasion wear resistance. Proc Int Therm Spray Conf 2000;10:575–82.

[14] Maurer C, Schulz U. Erosion resistant titanium based PVD coatings on CFRP. Wear 2013;302:937–45. https://doi.org/10.1016/j.wear.2013.01.045.

[15] Xu Z, Tian Y, Liu X, Yang R, Li H, Chen X. Microstructure evolution of the laser surface melted WC-Ni coatings exposed to cavitation erosion. Tribol Int 2022;173:107615. https://doi.org/10.1016/j.triboint.2022.107615.

[16] Zhou Y, Sun ZP, Yu Y, Li L, Song JL, Xie FQ, et al. Tribological behavior of Ni–SiC composite coatings produced by circulating-solution electrodeposition technique. Tribol Int 2021;159:106933. https://doi.org/10.1016/j.triboint.2021.106933.

[17] Domínguez-Ríos C, Hurtado-Macias A, Torres-Sánchez R, Ramos MA, González-Hernández J. Measurement of mechanical properties of an electroless Ni-B coating using nanoindentation. Ind Eng Chem Res 2012;51:7762–8. https://doi.org/10.1021/ie201760g.

[18] Kaya B, Gulmez T, Demirkol M, Preparation A, Samples T. Bath CECN. Preparation and properties of electroless Ni-B and Ni-B nanocomposite coatings. Proc World Congr Eng Comput Sci 2008:1–5.

[19] Zhang W, Ji C, Li B. Synthesis and properties of Ni–W/ZrO 2 nanocomposite coating fabricated by pulse electrodeposition. Results Phys 2019;13:102242. https://doi.org/10.1016/j.rinp.2019.102242.

[20] Hou KH, Chen YC. Preparation and wear resistance of pulse electrodeposited Ni-W/Al 2 O 3 composite coatings. Appl Surf Sci 2011;257:6340–6. https://doi.org/10.1016/j.apsusc.2011.01.089.

[21] Miyoshi K, Sutter JK, Mondry RJ, Bowman C, Ma K, Horan RA, et al. Measurements of erosion volume loss on bare and coated polymer matrix composites. Development 2003;L:22.

[22] Tabatabaei F, Vardak S, Alirezaei S, Raeissi K. The tribocorrosion behavior of Ni-P and Ni-P-ZrO2 coatings. Kov Mater 2018;56:379–87. https://doi.org/10.4149/km-2018-6-379.

[23] Wang Y, Shu X, Wei S, Liu C, Gao W, Shakoor RA, et al. Duplex Ni–P–ZrO2/Ni–P electroless coating on stainless steel (https://doi.org/) J Alloy Compd 2015;630:189–94. https://doi.org/10.1016/j.jallcom.2015.01.064.

[24] Sliem MH, Shahzad K, Sivaprasad VN, Shakoor RA, Abdullah AM, Fayyaz O, et al. Enhanced mechanical and corrosion protection properties of pulse electrodeposited NiP-ZrO2 nanocomposite coatings (https://doi.org/) Surf Coat Technol 2020;403:126340. https://doi.org/10.1016/j.surfcoat.2020.126340.

[25] Mudgal D, Sharma S, Bansal V, Sharma A. Investigation of corrosion, orrosion, hardness and wear resistant of electroless e ZrO2 nano-composite coatings 2017;5:6–9.

[26] Szczygieł B, Turkiewicz A, Serafińczuk J. Surface morphology and structure of Ni-P, Ni-P-ZrO2, Ni-W-P, Ni-W-P-ZrO2 coatings deposited by electroless method. Surf Coat Technol 2008;202:1904–10. https://doi.org/10.1016/j.surfcoat.2007.08.016.

[27] Shakoor RA, Bahgat Radwan A. Remarkable improvement in properties of NI-B coatings by the addition of mixed oxide nanoparticles. Mater Sci Technol Conf Exhib 2015;1:171–8. MS T 2015 2015.

[28] Hutchings I, Shipway P. Tribology: Friction and Wear of Engineering Materials. Butterworth-Heinemann; 2017.

[29] Fayyaz O, Khan A, Shakoor RA, Hasan A, Yusuf MM, Montemor MF, et al. Enhancement of mechanical and corrosion resistance properties of electrodeposited Ni–P–TiC composite coatings. Sci Rep 2021;11:5327. https://doi.org/10.1038/s41598-021-84716-6.

[30] Xia F, Xu H, Liu C, Wang J, Ding J, Ma C. Microstructures of Ni-AlN composite coatings prepared by pulse electrodeposition technology. Appl Surf Sci 2013;271:7–11. https://doi.org/10.1016/j.apsusc.2012.12.064.

[31] Yan C, Li H, Li J, Tong W, Kang Y, Xiong D. Synthesis of Ni-Al-ZrO2(Y2O3) composite coatings with excellent wear resistance through mechanical alloying combined with pulse electrodeposition. Ceram Int 2019;45:23798–803. https://doi.org/10.1016/j.ceramint.2019.07.288.

[32] Xia F, Li Q, Ma C, Liu W, Ma Z. Preparation and wear properties of Ni/TiN–SiC nanocoatings obtained by pulse current electrodeposition. Ceram Int 2020;46:7961–9. https://doi.org/10.1016/j.ceramint.2019.12.017.

[33] Hu R, Su Y, Liu Y, Liu H, Chen Y, Cao C, et al. Deposition process and properties of electroless Ni-P-Al2O3 composite coatings on magnesium alloy. Nanoscale Res Lett 2018;13:2–9. https://doi.org/10.1186/s11671-018-2608-0.

[34] Zoikis-Karathanasis A, Pavlatou EA, Spyrellis N. Pulse electrodeposition of Ni-P matrix composite coatings reinforced by SiC particles. J Alloy Compd 2010;494:396–403. https://doi.org/10.1016/j.jallcom.2010.01.057.

[35] Balaraju JN, Sankara Narayanan TSN, Seshadri SK. Structure and phase transformation behaviour of electroless Ni-P composite coatings. Mater Res Bull 2006;41:847–60. https://doi.org/10.1016/j.materresbull.2005.09.024.

[36] Shi P, Yi G, Wan S, Sun H, Feng X, Pham ST, et al. High temperature tribological performance of nickel-based composite coatings by incorporating multiple oxides (TiO2–ZnO–MoO3). Tribol Int 2021;155:106759. https://doi.org/10.1016/j.triboint.2020.106759.

[37] Bhutta MU, Khan ZA. Wear and friction performance evaluation of nickel based nanocomposite coatings under refrigerant lubrication. Tribol Int 2020;148:106312. https://doi.org/10.1016/j.triboint.2020.106312.

[38] Fayyad EM, Rasheed PA, Al-Qahtani N, Abdullah AM, Hamdy F, Sharaf MA, et al. Microbiologically-influenced corrosion of the electroless-deposited NiP-TiNi – Coating. Arab J Chem 2021;14:103445. https://doi.org/10.1016/J.ARABJC.2021.103445.

[39] Fayyaz O, Bahgat Radwan A, Sliem MH, Abdullah AM, Hasan A, Shakoor RA. Investigating the properties of electrodeposited of Ni-P-ZrC nanocomposite coatings. ACS Omega 2021;6:33310–24. https://doi.org/10.1021/acsomega.1c03117.

[40] Astm. G76–07, Standard Test Method for Conducting Erosion Tests by Solid Particle Impingement Using Gas Jets. ASTM Int 2013;i:1–6. https://doi.org/10.1520/G0076–18.2.

[41] Ruff AW, Ives LK. Measurement of solid particle velocity in erosive wear (https://doi.org/) Wear 1975;35:195–9. https://doi.org/10.1016/0043-1648(75)90154-4.

[42] Nguyen VB, Nguyen QB, Zhang YW, Lim CYH, Khoo BC. Effect of particle size on erosion characteristics. Wear 2016;348–349:126–37. https://doi.org/10.1016/j.wear.2015.12.003.

[43] Bahgat Radwan A, Ali K, Shakoor RA, Mohammed H, Alsalama T, Kahraman R, et al. Properties enhancement of Ni-P electrodeposited coatings by the incorporation of nanoscale Y2O3 particles (https://doi.org/) Appl Surf Sci 2018;457:956–67. https://doi.org/10.1016/j.apsusc.2018.06.241.

[44] Song Y, Yeon J, Na B. Numerical simulations of the hall-petch relationship in aluminium using gradient-enhanced plasticity model. Adv Civ Eng 2019;2019. https://doi.org/10.1155/2019/7356581.

[45] Czagány M, Baumli P, Kaptay G. The influence of the phosphorous content and heat treatment on the nano-micro-structure, thickness and micro-hardness of electroless Ni-P coatings on steel. Appl Surf Sci 2017;423:160–9. https://doi.org/10.1016/j.apsusc.2017.06.168.

[46] Taheri R, Oguocha INA, Yannacopoulos S. The tribological characteristics of electroless NiP coatings. Wear 2001;249:389–96. https://doi.org/10.1016/S0043-1648(01)00539-7.

[47] MacLean M, Farhat Z, Jarjoura G, Fayyad E, Abdullah A, Hassan M. Fabrication and investigation of the scratch and indentation behaviour of new generation Ni-P-nano-NiTi composite coating for oil and gas pipelines. Wear 2019;426–427:265–76. https://doi.org/10.1016/j.wear.2019.01.058.

[48] Gutsev D, Antonov M, Hussainova I, Grigoriev AY. Effect of SiO2 and PTFE additives on dry sliding of NiP electroless coating. Tribol Int 2013;65:295–302. https://doi.org/10.1016/j.triboint.2012.12.012.

[49] Ahmadiyeh S, Rasooli A, Hosseini MG. Ni–B/SiC nanocomposite coating obtained by pulse plating and evaluation of its electrochemistry and mechanical properties. Surf Eng 2019;35:861–72. https://doi.org/10.1080/02670844.2018.1498823.

[50] Li Z, Farhat Z, Islam MA. Investigation of single-particle erosion behavior of electroless Ni-P-Ti composite coatings. J Mater Eng Perform 2020;29:1671–85. https://doi.org/10.1007/s11665-020-04722-z.

[51] MacLean M, Farhat Z, Jarjoura G, Fayyad E, Abdullah A, Hassan M. Erosion and toughening mechanisms of electroless Ni-P-Nano-NiTi composite coatings on API X100 steel under single particle impact. J Surf Eng Mater Adv Technol 2019;09:88–106. https://doi.org/10.4236/jsemat.2019.94007.

[52] Goretta KC, Routbort JL, Mayer A, Schwarz RB. Erosion of amorphous nickelc-phosphorus. J Mater Res 1987;2:818–26. https://doi.org/10.1557/JMR.1987.0818.

[53] Islam MA, Farhat ZN. Effect of impact angle and velocity on erosion of API X42 pipeline steel under high abrasive feed rate. Wear 2014;311:180–90. https://doi.org/10.1016/j.wear.2014.01.005.

[54] Levy AV, Chik P. The effects of erodent composition and shape on the erosion of steel. Wear 1983;89:151–62. https://doi.org/10.1016/0043-1648(83)90240-5.

[55] Mishra SB, Prakash S, Chandra K. Studies on erosion behaviour of plasma sprayed coatings on a Ni-based superalloy. Wear 2006;260:422–32. https://doi.org/10.1016/j.wear.2005.02.098.

[56] Laguna-Camacho JR, Cruz-Mendoza LA, Anzelmetti-Zaragoza JC, Marquina-Chávez A, Vite-Torres M, Martínez-Trinidad J. Solid particle erosion on coatings employed to protect die casting molds. Prog Org Coat 2012;74:750–7. https://doi.org/10.1016/j.porgcoat.2011.09.022.

[57] Birnbaum HK. Mechanics of hydrogen related fracture of metals. Acta Met 1989;37:1407–13.

[58] Franco M, Sha W, Aldic G, Malinov S, Çimenoğlu H. Effect of reinforcement and heat treatment on elevated temperature sliding of electroless Ni–P/SiC composite coatings. Tribol Int 2016;97:265–71. https://doi.org/10.1016/j.triboint.2016.01.047.

[59] Senapati P, Sutar H, Murmu R, Bajpai S. Experimental design of solid particle wear behavior of ni-based composite coatings. J Compos Sci 2021;5:1–19. https://doi.org/10.3390/jcs5050133.

[60] Vasudev H, Thakur L, Singh H, Bansal A. Effect of addition of Al2O3 on the high-temperature solid particle erosion behaviour of HVOF sprayed Inconel-718 coatings. Mater Today Commun 2022;30:103017. https://doi.org/10.1016/j.mtcomm.2021.103017.

[61] Alirezaei S, Monirvaghefi SM, Saatchi A, Ürgen M, Kazmanlı K. Novel investigation on tribological properties of Ni–P–Ag–Al2O3 hybrid nanocomposite coatings. Tribol Int 2013;62:110–6. https://doi.org/10.1016/j.triboint.2013.01.022.